Room Acoustic Simulations using High-Order Spectral Element Methods

Finnur Pind[1,2], Mikael Staugaard Mejling[3], Allan P. Engsig-Karup[3], Cheol-Ho Jeong[2], Jakob Strømann-Andersen[1]

1) Henning Larsen, Copenhagen, Denmark.

2) Acoustic Technology group, Department of Electrical Engineering, Technical University of Denmark, Lyngby, Denmark.

3) Scientific Computing group, Department of Applied Mathematics and Computer Science, Technical University of Denmark, Lyngby, Denmark.

Summary

A wave-based numerical scheme for simulating room acoustics, based on the spectral element method, is presented. This method possesses qualities, such as high-order accuracy and geometrical flexibility, which make it very suitable for accurate and cost-effective room acoustic simulations of complex geometries of any size and shape. Various numerical experiments are carried out in order to analyze the accuracy and efficiency of the scheme. The results demonstrate how using high-order elements is essential for capturing wave dispersion and thereby allowing for the usage of coarser spatial discretizations, which can reduce computation time significantly. Furthermore, the methods ability to accurately represent curved boundaries, by means of curvilinear mesh elements, is demonstrated. The investigation is relevant for understanding how to improve the accuracy of room acoustics simulations in real geometries and serves as a stepping stone towards developing a relatively fast and flexible wave-based room acoustic simulator.

PACS no. 43.55.Ka, 43.58.Ta

1. Introduction

The subject of computer simulations of room acoustics dates back to the 1960's [1, 2] and since the 1990's, commercial software for room acoustic simulations has been readily available [3]. Since the acoustic performance of almost all real rooms is difficult or almost impossible to predict with sufficient accuracy without resorting to computer simulations, these software packages have become essential tools for most practicing room acousticians and other building designers involved with room acoustics [4].

The algorithms which are used for simulating acoustic sound propagation and reflection within rooms are typically divided into two main categories, namely the "geometrical" approach and "wave-based" approach. Examples of geometrical methods include the ray tracing method [5], the image source method [6] and the beam tracing method [7]. Geometrical algorithms are usually relatively fast, but the accuracy is often insufficient [8]. Particularly, in cases where wave phenomena, such as diffraction, interference, phase and scattering are a prominent part of the acoustic response of the room. Diffraction, [perceptually noticeable] interference and phase will mainly arise in small and medium sized spaces, and at low-mid frequencies. However, there are also well known cases of large spaces where geometrical methods cannot account for certain acoustic phenomena, such as the seat-dip effect [9] and in cases where acoustic focusing is prominent [10]. Most room acoustic software which use geometrical methods have some methods to account for surface scattering. Here the room surfaces are usually assigned scattering coefficients, but typically these coefficients are guesstimated based on crude visual inspections. There is still ongoing active research and development of geometrical algorithms, see [11, 12, 13] for examples of discussions of state of the art geometrical room acoustic algorithms.

Wave-based methods solve the governing acoustical equations numerically, usually either the wave equation or the equivalent linearized Euler equations. By solving the acoustical equations directly, all acoustic phenomena are inherently accounted for and these methods therefore allow for greater accuracy than their geometrical counterparts [8]. The drawback is that these methods come with a much higher computational cost than the geometrical methods. Exam-

ples of wave-based methods that have been used for simulating room acoustics include the finite-difference time-domain method (FDTD) [14], the finite element method (FEM) [15], the boundary element method (BEM) [16], the finite volume method (FVM) [17] and the pseudospectral time-domain method (PSTD) [18].

In this paper a high-order numerical scheme for simulating room acoustics, based on the spectral element method (SEM), is presented. High-order methods have not received much attention in the room acoustics community, although see recent papers [19, 20], where high-order FDTD methods are investigated. In short, high-order numerical methods have the ability to be much more computationally efficient than the typical low-order methods (such as FEM, BEM and "classic" FDTD), because they can solve the problem at hand using a much coarser grid or mesh than is required when using the low-order methods, enabling a significant reduction in the size of the computational problem [21].

The spectral element method [22] has many attractive features for room acoustic simulations, the two principal features being its high-order accuracy/efficiency and its geometric flexibility. It can be seen as an ideal mixture of the highly accurate spectral methods and the highly flexible finite element method [23]. The geometrical flexibility refers to the fact that the method can solve problems on meshes with elements of arbitrary shapes and sizes, and even mesh elements with curvilinear edges, which is an essential feature for accurately simulating rooms with complex geometries [24]. The popular FDTD method can certainly be extended to high-order accuracy, but it is difficult to use that method for geometries which do not fit a Cartesian grid [20].

The paper is organized as follows. A brief outline of the numerical scheme is presented in section 2. Section 3 contains results of various 2D and 3D numerical experiments, which illustrate the high accuracy and efficiency of the scheme presented. Finally some concluding remarks are made in section 4.

2. Numerical discretization

2.1. Governing equations

The sound field in a space is described by the linearized Euler euqations, which is the starting point of the discretization process:

$$\begin{aligned} \mathbf{v}_t &= -\frac{1}{\rho}\nabla p, \\ p_t &= -\rho c^2 \nabla \cdot \mathbf{v}, \end{aligned} \tag{1}$$

where $p(\mathbf{x},t)$ is the pressure, $\mathbf{v}(\mathbf{x},t)$ is the particle velocity, ρ is the density of the medium and c is the speed of sound in air (here $\rho = 1.2\,\mathrm{kg/m^3}$ and $c = 343\,\mathrm{m/s}$). In this study the numerical scheme will be implemented in both two and three dimensions. In room acoustics it is obviously the 3D case which is most relevant, but using 2D allows for some interesting and relevant test cases, which will be presented in sections 3.1 and 3.2, along with 3D simulations in sections 3.3 and 3.4.

In this study, only perfectly rigid boundary conditions will be used, defined as

$$\hat{\mathbf{n}} \cdot \mathbf{v} = 0 \quad \text{on } \partial\Omega. \tag{2}$$

The governing equations (eq. 1), with the boundary condition (eq. 2) incorporated, are rewritten on a weak formulation form as follows

$$\begin{aligned} \int_\Omega \mathbf{v}_t \ \phi \ \mathrm{d}\Omega &= -\frac{1}{\rho}\int_\Omega \nabla p \ \phi \ \mathrm{d}\Omega, \\ \int_\Omega p_t \ \phi \ \mathrm{d}\Omega &= \rho c^2 \int_\Omega \mathbf{v} \cdot \nabla\phi \ \mathrm{d}\Omega. \end{aligned} \tag{3}$$

This weak formulation can then discretized, as described briefly here below. Details are omitted for the sake of brevity, see references for further implementation details.

2.2. Spatial discretization

The domain Ω is divided into a set of non-overlapping elements $e^{(n)}$, $n = 1 \dots N$. Each element is then covered by a set of nodes, making up a total of M nodes on the mesh and having coordinates $\mathbf{x}_i$, $i = 1 \dots M$. In 2D triangular elements are used and in 3D hexahedral elements are used, although in theory elements of any shape could be used. To be able to represent the global solution $p(\mathbf{x},t)$ and $\mathbf{v}(\mathbf{x},t)$ by some approximate solutions constructed from polynomial basis functions of order P, each element must contain $M_P = (P+1)(P+2)/2$ nodes in 2D for the triangular elements and $M_P = (P+1)^3$ nodes in 3D for the hexahedral elements. Figure 1 shows an example of a meshed 2D domain, supporting $P = 1$ basis functions (i.e. a FEM mesh), whereas figure 2 shows an example of a 2D mesh supporting high-order $P = 4$ basis functions.

The unknown functions $\mathbf{v}$ and p in eq. (3) are represented by piece-wise polynomial functions on the form

$$\begin{aligned} \mathbf{v}(\mathbf{x},t) &\approx \sum_{i=1}^{M} \hat{\mathbf{v}}_i(t) N_i(\mathbf{x}), \\ p(\mathbf{x},t) &\approx \sum_{i=1}^{M} \hat{p}_i(t) N_i(\mathbf{x}), \end{aligned} \tag{4}$$

where $\hat{p}_i(t), \hat{\mathbf{v}}_i(t)$ are the values of p and $\mathbf{v}$ at the i'th node at time t and N_i are global basis functions, defined such that they possess the Cardinal property, $N_i(x_j) = \delta_{ij}$ where δ_{ij} is the Kronecker delta function.

The *global* basis functions can then be represented in terms of *local* nodal basis functions defined on each

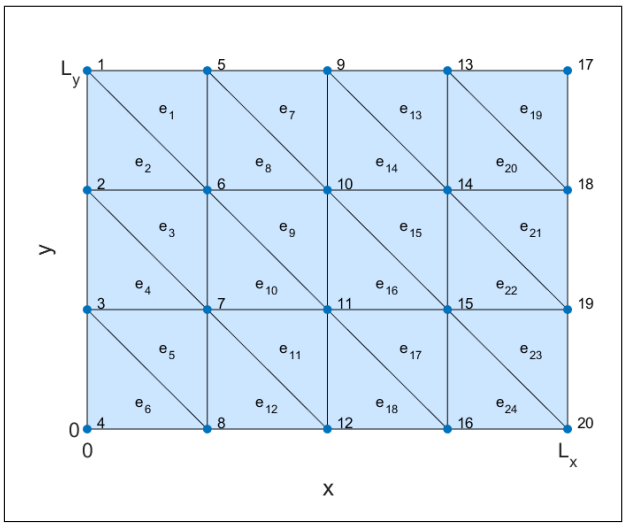

Figure 1. A 2D mesh of a rectangular domain, using triangular elements and supporting $P = 1$ basis functions. Here $N = 24$ and $M = 20$.

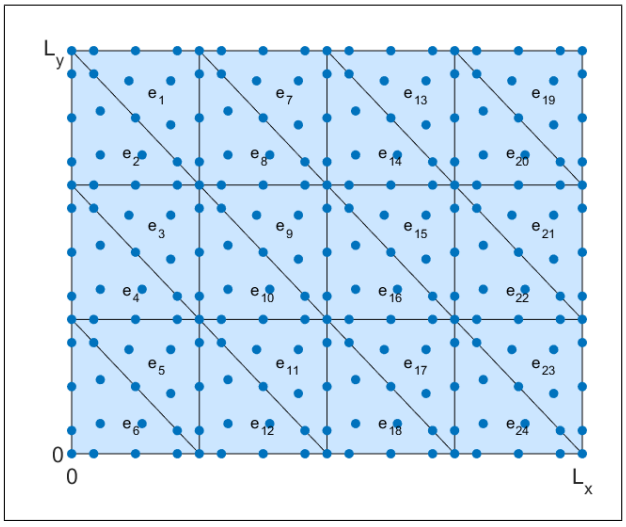

Figure 2. An example of a 2D mesh of a rectangular domain, using triangular elements and nodes for defining the $P = 4$ basis functions. Here $N = 24$ and $M = 360$.

element,

$$N_i(\mathbf{x}) = \bigoplus_{n=1}^{N} \sum_{j=1}^{M_P} N_j^{(n)}(\mathbf{x}_i) N_j^{(n)}(\mathbf{x}), \quad \mathbf{x} \in \Omega^{(n)}, \quad (5)$$

where $\bigoplus$ is the direct sum operator and $N_j^{(n)}(\mathbf{x})$ are the local local basis functions, taken to be Lagrange polynomials, belonging to the n'th element and defined from the set of nodes associated with that particular element.

By further substituting the approximations in eq. (4) for $\mathbf{v}$ and p into eq. (3) and setting the test function ϕ equal to $N_i, i = 1 \dots M$, one arrives at the following set of equations, written on matrix form (shown here for the three dimensional case):

$$\begin{aligned} M\hat{u}' &= -\frac{1}{\rho} S_x \hat{p}, \\ M\hat{v}' &= -\frac{1}{\rho} S_y \hat{p}, \\ M\hat{w}' &= -\frac{1}{\rho} S_z \hat{p}, \\ M\hat{p}' &= \rho c^2 \left(S_x^T \hat{u} + S_y^T \hat{v} + S_z^T \hat{w} \right), \end{aligned} \quad (6)$$

by defining the following matrix operators

$$\begin{aligned} M_{ij} &= \int_\Omega N_j \; N_i \; \mathrm{d}\Omega, \\ S_{x,(ij)} &= \int_\Omega (N_j)_x \; N_i \; \mathrm{d}\Omega, \\ S_{y,(ij)} &= \int_\Omega (N_j)_y \; N_i \; \mathrm{d}\Omega, \\ S_{z,(ij)} &= \int_\Omega (N_j)_z \; N_i \; \mathrm{d}\Omega. \end{aligned} \quad (7)$$

In finite element terminology, M is typically called the mass matrix and S is called the stiffness matrix. Once these matrices have been determined, what remains is simply to solve an ODE system. In order to determine these matrices, it is convenient to introduce the concept of an *element matrix*.

The integrals in (7) are only non-zero when the nodes i, j are adjacent in the mesh. This means that each element $e^{(n)}$ in the mesh only contributes to entries M_{ij} when $\mathbf{x}_i, \mathbf{x}_j \in e^{(n)}$. This leads to the definition of the element mass matrix as (see further details in e.g. [23, 25])

$$\mathcal{M} = \left(\mathcal{V}\mathcal{V}^T \right)^{-1}, \quad (8)$$

where $\mathcal{V}$ is a generalized Vandermonde matrix. Similarly, the element stiffness matrix is defined as (one in each dimension)

$$\mathcal{S}_r = \mathcal{M}\mathcal{D}_r, \quad (9)$$

where

$$\mathcal{D}_r = \mathcal{V}_r \mathcal{V}^{-1}, \quad (10)$$

is a nodal differentiation matrix. Here, the orthonormality of modal basis functions applied in the derivation, ensures that discrete quadrature rules in the construction of the element matrices can be avoided.

These element matrices, which represent certain reference elements (typically a unit triangle or a unit square), can then be transformed to represent mesh elements of arbitrary size, shape and location, even curvilinear elements. The final step is then to assemble the global matrices in eq. (7) by iterating over the elements and summing the element contributions from the element matrices.

2.3. Time Discretization and temporal stability

For the time integration, an explicit fourth order Runge-Kutta time integration method is applied [26]. Explicit time stepping schemes come with conditional stability which sets an upper bound on the temporal step size, in the form of the global CFL condition

$$\Delta t \leq \frac{C_1}{\max_i |\lambda_i|}, \tag{11}$$

where λ_i represents the eigenvalues of the spatial discretization. The constant C_1 is of the order $\mathcal{O}(1)$. For the fourth order Runge-Kutta time integration method it can be shown that $C_1 = 2\sqrt{2}$ for problems with purely imaginary eigenspectrums, such as hyperbolic problems without losses, as is the case here [27].

A known drawback of the spectral element method is the fact that the eigenvalues λ_i have an unattractive scaling with respect to polynomial order P, of the form $\max_i |\lambda_i| \sim C_2 P^{2\gamma}$, where γ is the highest order of differentiation in the governing equations and the constant C_2 is dependent on the minimum mesh size for an element in the mesh [23]. This means that using very high polynomial basis function orders P results in only marginal benefits in efficiency due to a severe restriction on the temporal step size Δt. In comparison, for FDTD, the eigenvalue scaling is on the more favorable form of $\max_i |\lambda_i| \sim C_3 P^{\gamma}$ [28]. This means that the geometrical flexibility of the SEM method, compared to the Cartesian nature of FDTD, comes with some cost.

In the 2D and 3D numerical experiments presented in this paper, the temporal step size is determined in the following way. In 2D, where triangular elements are used, a method from [29] is applied, where the temporal step size is given by

$$\Delta t = C_{\mathrm{CFL}} \min(\Delta r_i) \min \frac{r_D}{c}, \tag{12}$$

where Δr_i is the grid spacing between Gauss-Lobatto nodes in the 1D reference element $I = [-1, 1]$ and r_D is the radius of the triangular elements' inscribed circle. The constant C_{CFL} is chosen such that the stability criterion (eq. (11)) is fulfilled. In all 2D numerical experiments in this study it is taken to be $C_{\mathrm{CFL}} = 0.75$.

In the 3D case, where hexahedral elements are used, the temporal step size is given by

$$\Delta t = C_{\mathrm{CFL}} \frac{\min(\Delta x\, \Delta y\, \Delta z)}{c}, \tag{13}$$

where $\Delta x, \Delta y$ and Δz are the grid spacings between nodes on the mesh in each dimension. Again, the constant C_{CFL} should be chosen such that the stability criterion is fulfilled.

2.4. Interpolation and mass lumping

To be able to extract simulated sound pressure values with high-order accuracy not only in the nodes of the mesh, but in an arbitrary location in the domain, interpolation can be used. This can be done by means of an interpolation operator, which is defined as

$$\mathcal{I}_p = \mathcal{V}_k \mathcal{V}^{-1}, \tag{14}$$

where $\mathcal{V}_k$ is a Vandermonde "point" matrix, based on the coordinates of the receiver, mapped to the reference element and $\mathcal{V}$ is the generalized element Vandermonde matrix. The simulated sound pressure in the receiver location is then given by

$$p = \mathcal{I}_p p_k, \tag{15}$$

where p_k is the simulated sound pressure in the nodes of the element containing the receiver.

Mass lumping techniques can be used to improve the efficiency of the scheme, by converting the global mass matrix M in eq. (7) into a diagonal matrix. The benefits of using mass lumping in finite element methods are well known and well documented [30]. The use of mass lumping will reduce accuracy slightly, but global convergence rates are maintained [31] and since the computational load is significantly reduced, the loss in accuracy can easily be compensated by slightly increasing the amount of degrees of freedom on the mesh, while maintaining a net improvement in efficiency.

The mass lumping approach is used in this study in the 3D scheme only. In this case, since the 3D mesh used is based on hexahedral elements, the mass lumping is straightforward, namely

$$A_{ij} = \mathrm{diag}\left(\sum_j A_{ij}\right). \tag{16}$$

3. Numerical experiments

3.1. 2D rectangular domain

The first test case presented here is that of a 2D 1×1 m square domain with perfectly reflecting boundaries. The frequency response of this domain is simulated using four different polynomial orders (P=1,2,4,6), but in all cases the total number of DOF's on the mesh is kept the same (169 nodes), i.e. same level of "fineness" of the spatial discretization. This means that the size of the matrix operators in eq. (6) is the same for all orders. Figure 3 shows the meshes used for the different orders tested, along with the source and receiver positions. The simulation is started with a Gaussian pulse pressure initial condition with a spatial variance of $0.05\,\mathrm{m}^2$. The integration time is taken to be 3 s (note that in theory a perfectly reflecting domain with no losses has an infinite impulse response

length, here the response is simply cut off after 3 seconds).

Figure 4 shows the simulated frequency responses. From the figure it is clear how the high-order methods result in significantly more accurate predictions of the analytical modal frequencies, even though the spatial discretization is equally fine in all cases. This clearly illustrates the key benefit of high-order methods, i.e. how they allow for using a much coarser spatial discretization and thus result in a considerable improvement in computational efficiency. Remember that the P=1 case corresponds to the traditional FEM method – using this method to match the accuracy (or frequency range) of the $P = 6$ case would require a vastly finer discretization, which of course leads to a much larger computational problem.

However, note that when higher polynomial orders are used, a smaller temporal step size must be used (due to eigenvalue scaling, as discussed in section 2.3). This effectively sets an upper limit on how high the polynomial order can be, while still observing improvements in efficiency. In our ongoing work, we are doing a rigorous analysis of just exactly how much more efficient the high-order methods are, while also trying to determine what could be the optimal polynomial order for room acoustic simulations using SEM. Initial results of this analysis indicate that for 3D room acoustic simulations, the high-order methods can be vastly more efficient than their low-order counterparts (on the order of 100-1,000,000 times faster), depending on the desired level of numerical accuracy, the desired frequency range and the desired simulation integration time (impulse response length). The more accurate, the higher the frequency range and the longer the integration time is desired, the larger the gains of using high-order method become [21]. Furthermore, our initial results seem to indicate that polynomial orders in the range of 3-6 could be optimal. However, these numbers mentioned here should be taken with a grain of salt, since the efficiency analysis work is not yet complete.

3.2. 2D circular domain

Consider now the case of a 2D circular domain, with radius 0.5 m and with perfectly reflecting boundaries (see figure 5). This particular test case is chosen to illustrate the high geometric flexibility of the numerical scheme presented. Not only does the scheme work with unstructured meshes of arbitrary shapes (such as a typical finite element mesh), but it can also make use of elements with curvilinear edges, when high-order polynomials ($P > 2$) are used. When typical straight-sided mesh elements are employed to discretize the circular domain, the curved boundary of the domain will be poorly represented unless an extremely fine mesh is used. This will naturally introduce errors in the simulation, errors which will grow with increasing frequency.

The frequency response for the source-receiver pair shown in figure 5 is simulated for two cases. In both cases $P = 4$ basis functions are used, but in one case only straight-sided triangle mesh elements are used (the mesh shown in the figure), whereas in the other, the boundary edges of the boundary elements have been made curvilinear, by means of a transformation. Figure 6 contains the simulated frequency responses, which reveal that the straight-sided element approach introduces a considerable deviation from the true analytical modes (even though the spatial discretization used is quite fine in this case), especially at the higher frequencies. The figure also shows how the usage of curvilinear boundaries remedies the problem.

3.3. 3D Accuracy and dispersion properties

In order to analyze the numerical accuracy properties (error convergence) of the 3D scheme, a periodic cube domain can be used. A uniform mesh of hexahedral elements is employed. The model is excited by a sine wave initial pressure condition and the analytical solution is known. The numerical error is the the difference between the numerical solution and the analytical solution, expressed in the L_2 norm. The error will be a mixture of dissipation (amplitude) and dispersion (phase) errors. However, for the SEM scheme presented here, the errors are almost purely dispersive. Figure 7 shows the results of a convergence test for the 3D scheme for various polynomial basis function orders P. It shows the global error as a function of the inverse of the mesh element side length h.

The results of the convergence test show how high-order polynomial basis functions result in higher accuracy for a given element size on the mesh. This is in harmony with our 2D numerical experiments described above. For P even, a convergence rate of P is observed, but for P odd a convergence rate of $P + 1$ is observed. This is as expected for Galerkin SEM discretizations, and indicates that having P odd will probably yield more cost-effective results. Note also that when larger, but stable, time steps are used, as would almost certainly be the case in practice, the high convergence rates of the very high orders ($P \geq 6$) will be contaminated due to temporal errors of the Runge-Kutta time integration scheme, the degree of which will differ from case to case. This is another reason why very high orders for this particular scheme are not as practical as orders in the 3-6 range probably are.

3.4. 3D shoebox room

As a final proof-of-concept test case, the numerical scheme is used to simulate the frequency response of a small 3D cube room, again with perfectly reflecting boundaries. The simulation is set up in a similiar fashion as the 2D square case, i.e. for all the different polynomial orders tested, the total number of DOF's on the mesh are kept fixed. Again a Gaussian pulse

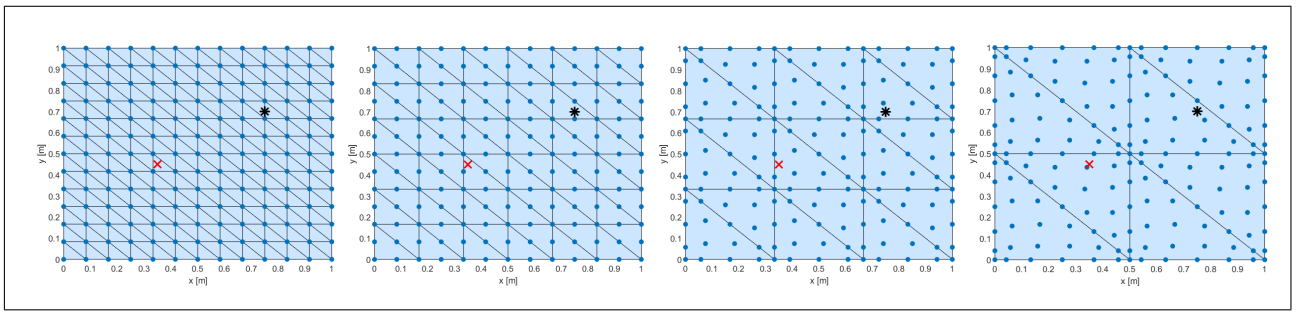

Figure 3. Meshes of the 2D rectangular domain used for the different orders tested. From left to right: $P = 1$, 288 elements. $P = 2$, 72 elements. $P = 4$, 18 elements. $P = 6$, 8 elements. In all cases the total degrees of freedom equals 169. Source location is shown with a red cross $(s_x, s_y) = (0.35, 0.45)$ m, and the receiver location is shown with a black star $(r_x, r_y) = (0.75, 0.70)$ m.

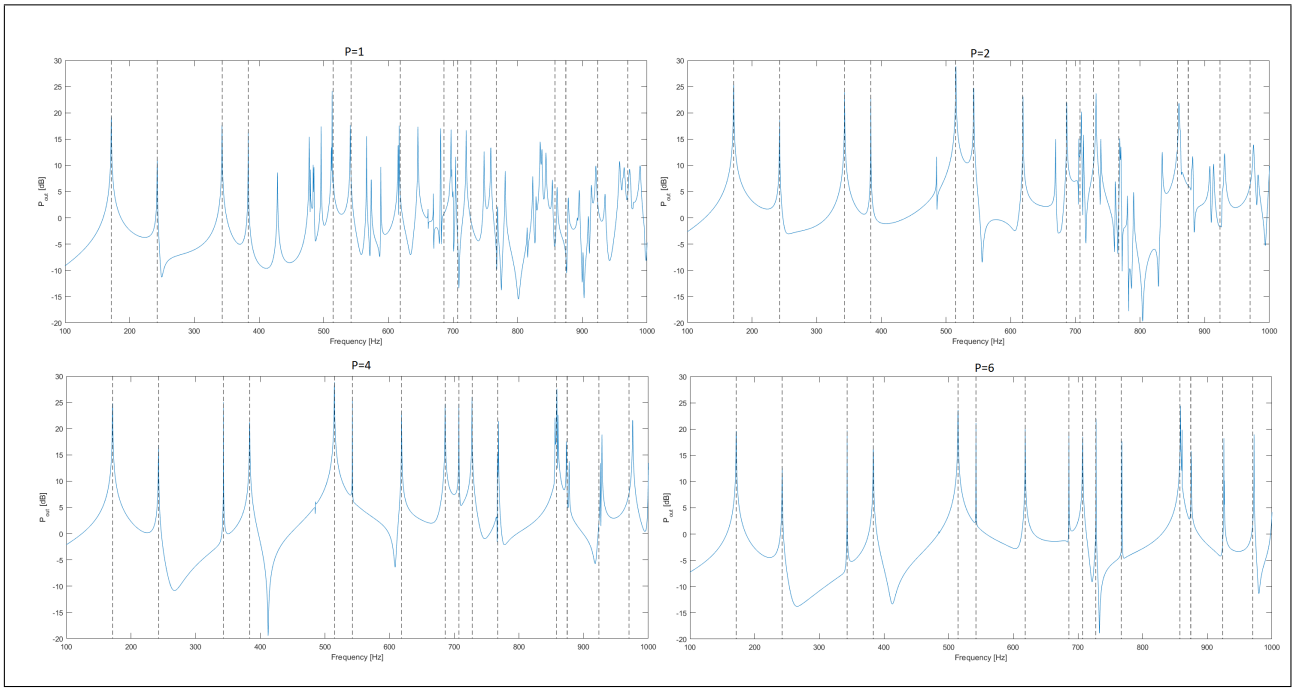

Figure 4. Simulated frequency responses of the 2D rectangle for the different orders tested. Analytic modes are shown as dashed vertical lines. Top left: $P = 1$, top right: $P = 2$, bottom left $P = 4$ and bottom right $P = 6$.

initial condition is used to initiate the simulation. The temporal step size used is determined with eq. 13 with $C_{\text{CFL}} = 0.75$.

Figure 8 contains the simulated frequency responses. As was seen for the 2D case, the high-order methods produce significantly more accurate simulation results than the low-order case, even though the same level of spatial discretization is used.

4. Conclusions

A wave-based numerical scheme, based on the spectral element method, for simulating room acoustics, has been presented. This scheme has the key benefits of a) high-order accuracy and b) a high level of geometrical flexibility. It has been shown, by various numerical experiments, how the high-order accuracy results in vastly more accurate simulation results for a given level of mesh fineness. This means that a much coarser spatial discretization can be used when the high-order basis functions are used, which will lead to significant improvements in efficiency. The geometrical flexibility of the scheme has also been illustrated, where the use of curvilinear boundary elements was shown to remove errors associated with typical straight-sided mesh elements.

Of course there are many issues that remain to be explored. As mentioned in the paper, there is currently ongoing a more thorough investigation into the efficiency properties of the scheme. Moreover, parallel implementations on modern many-core computer architectures will also be necessary to reduce computation times even further. Other avenues for further acceleration, such as local time stepping and matrix free implementations, remain an option. Naturally, it

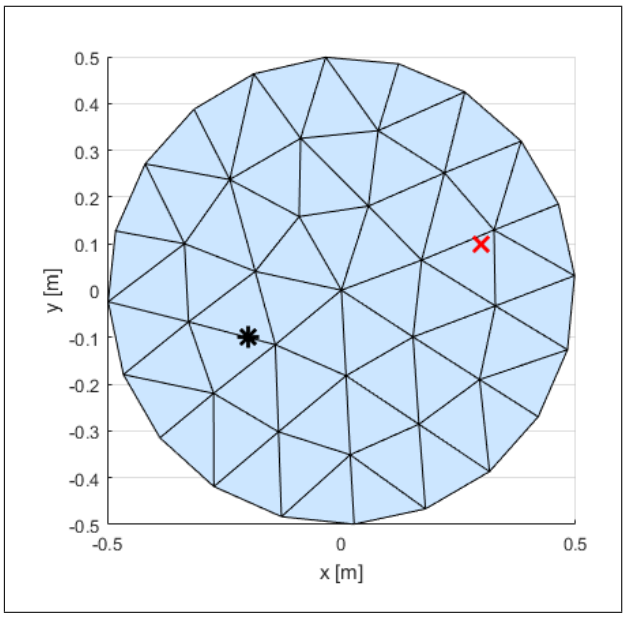

Figure 5. Experiment setup. 2D mesh with with 60 elements, 521 DOF's (supporting P=4 basis functions). Source location is shown with a red cross ($(s_x, s_y) = (0.3, 0.1)$) and the receiver location is shown with a black star ($(r_x, r_y) = (-0.2, -0.1)$).

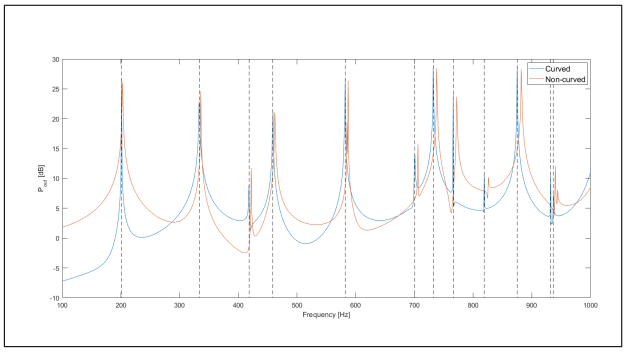

Figure 6. Simulated frequency response of 2D circle with and without curvilinear boundary elements. Analytic modes are shown as dashed vertical lines.

will be necessary to augment the scheme such that it can handle frequency dependent boundary conditions and viscous losses of the medium as well.

Acknowledgement

This research has been partially funded by the Innovation Fund in Denmark.

References

[1] M. R. Schroeder, K. H. Kuttruff: On Frequency Response Curves in Rooms. Comparison of Experimental, Theoretical, and Monte Carlo Results for the Average Frequency Spacing between Maxima. The Journal of the Acoustical Society of America (1962) 76-80.

[2] A. Krokstad, S. Strom, S. Soersdal: Calculating the Acoustical Room Response by the Use of a Ray Tracing Technique. Journal of Sound and Vibration (1968) 118-125.

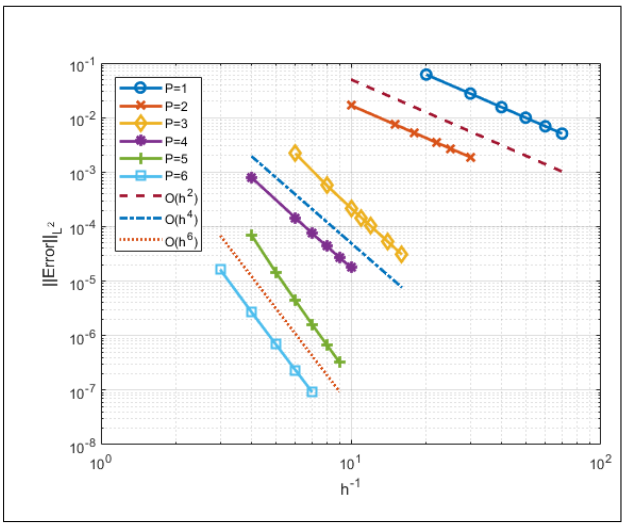

Figure 7. Convergence test for the 3D periodic domain problem. The time step in all simulations is set to be small enough such that spatial truncation errors dominate.

[3] G. M. Naylor: ODEON–Another Hybrid Room Acoustical Model. Applied Acoustics (1993) 131-143.

[4] M. Vorlander: Auralization: Fundamentals of Acoustics, Modelling, Simulation, Algorithms and Acoustic Virtual Reality. Springer, Berlin, 2008.

[5] A. Kulowski: Algorithmic Representation of the Ray Tracing Technique. Applied Acoustics (1985) 449-469.

[6] H. Lee, B.-H. Lee: An Efficient Algorithm for the Image Model Technique. Applied Acoustics (1988) 87-115.

[7] S. Laine, S. Siltanen, T. Lokki, L. Savioja: Accelerated Beam Tracing Algorithm. Applied Acoustics (2009) 172-181.

[8] M. Vorlander: Computer Simulations in Room Acoustics: Concepts and Uncertainties. The Journal of the Acoustical Society of America (2013) 1203-1213.

[9] J. LoVetri, D. Mardare, G. Soulodre: Modeling of the Seat Dip Effect Using the Finite-Difference Time-Domain Method. The Journal of the Acoustical Society of America (1996) 2204-2212.

[10] M. L. S. Vercammen: Sound Concentration Caused by Curved Surfaces. Eindhoven University of Technology, The Netherlands, 2011.

[11] G. Marbjerg, J. Brunskog, C.-H. Jeong, E. Nilsson: Development and Validation of a Combined Phased Acoustical Radiosity and Image Source Model for Predicting Sound Fields in Rooms. The Journal of the Acoustical Society of America (2015) 1457-1468.

[12] C.-H. Jeong, J.-G. Ih, J. H. Rindel: An Approximate Treatment of Reflection Coefficient in the Phased Beam Tracing Method for the Simulation of Enclosed Sound Fields at Medium Frequencies. Applied Acoustics (2008) 601-613.

[13] L. Savioja, U. P. Svensson: Overview of Geometrical Room Acoustic Modeling Techniques. The Journal of the Acoustical Society of America (2015) 708-730.

[14] D. Botteldooren: Finite-Difference Time-Domain Simulation of Low-Frequency Room Acoustic Problems. The Journal of the Acoustical Society of America (1995) 3302-3308.

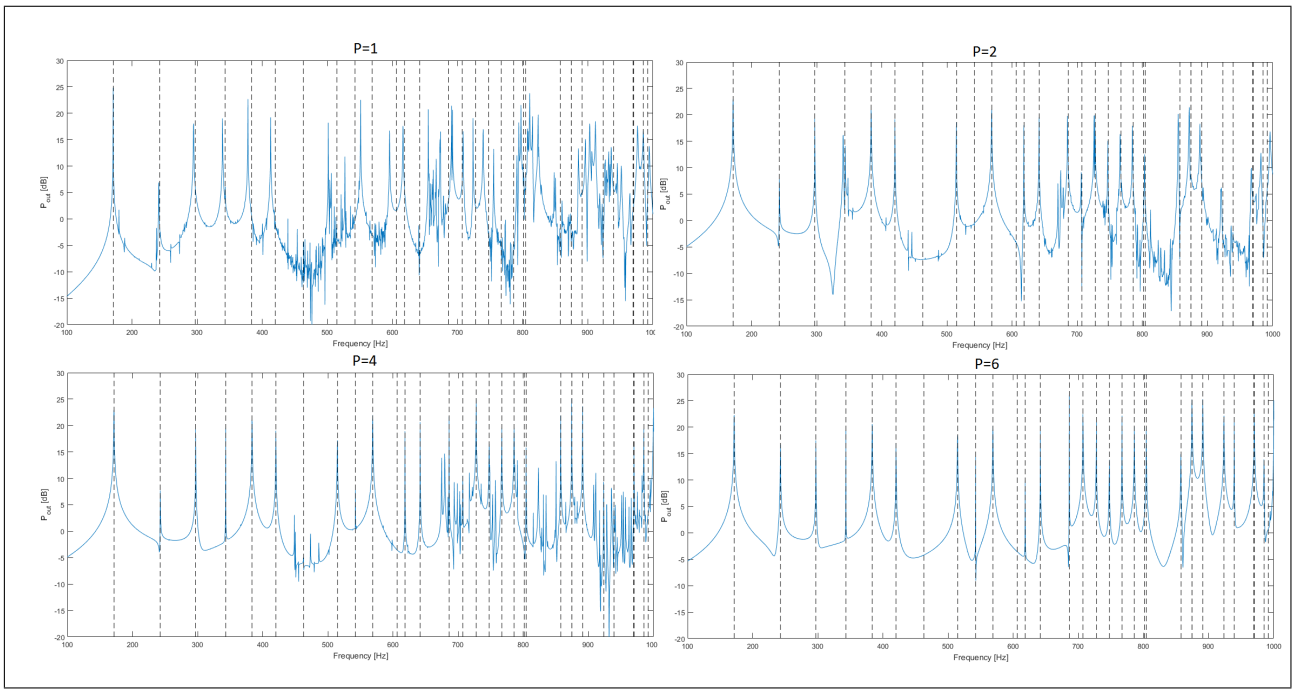

Figure 8. Simulated frequency responses of the 3D cube room for the different orders tested, while using fixed amount of DOF's on the mesh (15625 nodes). Analytic modes are shown as dashed vertical lines. The source location is $((s_x, s_y, s_z) = (0.25, 0.75, 0.60))$ and the receiver location is $((r_x, r_y, r_z) = (0.85, 0.30, 0.80))$. Top left: $P = 1$ (24 mesh elements per dimension), top right: $P = 2$ (12 mesh elements per dimension), bottom left $P = 4$ (6 mesh elements per dimension) and bottom right $P = 6$ (4 elements per dimension).

[15] W. Ahnert, M. Bansal, S. Feistel: Large Scale FEM Analysis of a Studio Room. Audio Engineering Society Convention 120 (2006).

[16] J. A. Hargreaves, T. J. Cox: A Transient Boundary Element Method Model of Schroeder Diffuser Scattering Using Well Mouth Impedance. The Journal of the Acoustical Society of America (2008) 2942-2951.

[17] S. Bilbao: Modeling of Complex Geometries and Boundary Conditions in Finite Difference/Finite Volume Time Domain Room Acoustics Simulation. IEEE Transactions on Audio, Speech, and Language Processing (2013) 1524-1533.

[18] M. Hornikx, T. Krijnen, L. van Harten: openPSTD: The Open Source Pseudospectral Time-Domain Method for Acoustic Propagation. Computer Physics Communications (2016) 298-308.

[19] J. van Mourik, D. Murphy: Explicit Higher-Order FDTD Schemes for 3D Room Acoustic Simulation. IEEE/ACM Transactions on Audio, Speech, and Language Processing (2014) 2003-2011.

[20] B. Hamilton, S. Bilbao: FDTD Methods for 3-D Room Acoustics Simulation With High-Order Accuracy in Space and Time. IEEE/ACM Transactions on Audio, Speech, and Language Processing (2017) 2112-2124.

[21] H.-O. Kreiss, J. Oliger: Comparison of Accurate Methods for the Integration of Hyperbolic Equations. Tellus (1972) 199–215.

[22] A. T. Patera: A Spectral Element Method for Fluid Dynamics: Laminar Flow in a Channel expansion. Journal of Computational Physics (1984) 468–488.

[23] A. P. Engsig-Karup, C. Eskilsson, D. Bigoni: A Stabilised Nodal Spectral Element Method for Fully Nonlinear water Waves. Journal of Computational Physics (2016) 1-21.

[24] S. Bilbao, B. Hamilton, J. Botts, L. Savioja: Finite Volume Time Domain Room Acoustics Simulation under General Impedance Boundary Conditions. IEEE/ACM Transactions on Audio, Speech, and Language Processing (2016) 161-173.

[25] A. P. Engsig-Karup: The Spectral/*hp*-Finite Element Method for Partial Differential Equations. Technical University of Denmark, 2016.

[26] R. LeVeque: Finite Difference Methods for Ordinary and Partial Differential Equations. Society for Industrial and Applied Mathematics, 2007.

[27] A. P. Engsig-Karup, L. S. Glimberg, A. S. Nielsen, O. Lindberg: Fast Hydrodynamics on Heterogenous Many-core Hardware, in: Raphäel Couturier (Ed.), Designing Scientific Applications on GPUs, in: Lecture Notes in Computational Science and Engineering, CRC Press / Taylor Francis Group, 2013.

[28] B. Fornberg: A Practical Guide to Pseudospectral Methods. Cambridge University Press. 1996.

[29] J. S. Hesthaven, T. Warburton: Nodal Discontinuous Galerkin Methods - Algorithms, Analysis, and Applications. Springer, New York, 2008.

[30] C. A. Felippa, Q. Guo, K. C. Park: Mass Matrix Templates: General Description and 1D Examples. Archives of Computational Methods in Engineering (2015) 1-65.

[31] I. Fried, D.S. Malkus: Finite Element Mass Matrix Lumping by Numerical Integration with no Convergence Rate Loss. International Journal of Solids and Structures (1975) 461-466.